Correction

MEDICAL SCIENCES, APPLIED PHYSICAL SCIENCES

Correction for "Label-free DNA imaging in vivo with stimulated Raman scattering microscopy," by Fa-Ke Lu, Srinjan Basu, Vivien Igras, Mai P. Hoang, Minbiao Ji, Dan Fu, Gary R. Holtom, Victor A. Neel, Christian W. Freudiger, David E. Fisher, and X. Sunney Xie, which appeared in issue 37, September 15, 2015, of *Proc Natl Acad Sci USA* (112:11624–11629; first published August 31, 2015; 10.1073/pnas.1515121112).

The authors note that the grant number DE-FG02-09ER16104 should instead appear as DE-SC0001548.

www.pnas.org/cgi/doi/10.1073/pnas.1519382112

Label-free DNA imaging in vivo with stimulated Raman scattering microscopy

Fa-Ke Lu[a,1], Srinjan Basu[b,1,2], Vivien Igras[c], Mai P. Hoang[d], Minbiao Ji[a], Dan Fu[a], Gary R. Holtom[a], Victor A. Neel[e], Christian W. Freudiger[a,3], David E. Fisher[c,4], and X. Sunney Xie[a,4]

[a]Department of Chemistry and Chemical Biology, Harvard University, Cambridge, MA 02138; [b]Department of Molecular and Cellular Biology, Harvard University, Cambridge, MA 02138; [c]Cutaneous Biology Research Center, Department of Dermatology, Massachusetts General Hospital, Harvard Medical School, Charlestown, MA 02129; [d]Department of Pathology, Massachusetts General Hospital, Harvard Medical School, Boston, MA 02114; and [e]Department of Dermatology, Massachusetts General Hospital, Harvard Medical School, Boston, MA 02114

Contributed by X. Sunney Xie, August 2, 2015 (sent for review April 16, 2015; reviewed by Daniel Côté and Hervé Rigneault)

Label-free DNA imaging is highly desirable in biology and medicine to perform live imaging without affecting cell function and to obtain instant histological tissue examination during surgical procedures. Here we show a label-free DNA imaging method with stimulated Raman scattering (SRS) microscopy for visualization of the cell nuclei in live animals and intact fresh human tissues with subcellular resolution. Relying on the distinct Raman spectral features of the carbon-hydrogen bonds in DNA, the distribution of DNA is retrieved from the strong background of proteins and lipids by linear decomposition of SRS images at three optimally selected Raman shifts. Based on changes on DNA condensation in the nucleus, we were able to capture chromosome dynamics during cell division both in vitro and in vivo. We tracked mouse skin cell proliferation, induced by drug treatment, through in vivo counting of the mitotic rate. Furthermore, we demonstrated a label-free histology method for human skin cancer diagnosis that provides comparable results to other conventional tissue staining methods such as H&E. Our approach exhibits higher sensitivity than SRS imaging of DNA in the fingerprint spectral region. Compared with spontaneous Raman imaging of DNA, our approach is three orders of magnitude faster, allowing both chromatin dynamic studies and label-free optical histology in real time.

stimulated Raman scattering microscopy | skin cancer | label-free histology | cell division | mitotic rate

In vivo imaging of chromatin or chromosome structures and dynamics during vital cellular processes, such as cell division, differentiation, apoptosis, and carcinogenesis, generally relies on the use of either exogenous or endogenous fluorescent labels, the latter of which often involves complicated transgenic organisms (1, 2). A label-free approach, however, allows the visualization of these processes in a noninvasive way in live organisms. In medicine, visualization of nuclear morphology, architecture, size, shape, and mitotic figures provide the most important cytologic features for rendering histologic diagnosis (3, 4). Conventional histology is heavily reliant on tissue biopsies and staining (such as H&E or immunohistochemistry), whereas label-free imaging is able to reveal similar information as that from the stained tissue, and in addition, it allows for a noninvasive characterization and diagnosis of human tissue in real time in vivo.

Stimulated Raman scattering (SRS) microscopy offers a contrast mechanism based on Raman spectroscopy, probing the intrinsic vibrational frequencies of chemical bonds or groups (5–8). In SRS microscopy, the collinear pump and Stokes laser beams, at frequencies of ω_p and ω_s, respectively, are tightly focused onto the sample (Fig. 1*A*). When the frequency difference, $\omega_p - \omega_s$, matches a Raman-active molecular vibration, the SRS signal (attenuation to the pump beam or increase on the Stokes beam) is generated through a nonlinear process similar to the stimulated emission. With a highly sensitive detection scheme, involving megahertz modulation transfer, SRS microscopy exhibits orders of magnitude of shorter acquisition time than conventional Raman microscopy (5). Being a nonlinear optical microscopy, it offers 3D sectioning capability with a diffraction-limited spatial resolution. SRS microscopy has been extensively applied to image biomolecules in cells and tissues (9–15).

SRS imaging was initially carried out at one Raman shift at a time (5). Recent developments on multiplex detection allow for distinguishing various chemical species with overlapping Raman bands by either broadband excitation (16, 17) or narrowband scanning (18, 19). SRS at two specific Raman shifts within the broadband of the carbon-hydrogen (CH) stretching vibrational mode (2,800–3,050 cm^{-1}) has been used to simultaneously map protein and lipid distribution in cells and tissues (20, 21). In particular, protein and lipid imaging has been applied to delineate brain tumor margins, providing images similar to conventional H&E staining (11). However, SRS does not offer detailed nuclear morphology and architecture, compared with the conventional histology, due to the lack of imaging contrast for DNA.

SRS has been demonstrated to be valuable for DNA imaging in cultured cells based on detection of the phosphate peaks within the fingerprint spectral region (22). However, imaging of DNA in this spectral region is difficult for cells in interphase because of the lower DNA density, especially in live tissue. This challenge is also the case for spontaneous Raman imaging (SI *Text*) (23).

Significance

Microscopic imaging of DNA has to rely on the use of fluorescent staining, an exogenous labeling in biological and biomedical studies, which often leads to uncertainty with respect to the quality and homogeneity of the staining. Label-free imaging of DNA will enable noninvasive visualization of live cell nuclei in both human and animals. Spontaneous Raman microspectroscopy offers label-free chemical contrast for DNA imaging; however, its slow imaging speed hampers its wide application for in vivo and dynamic studies. Here we developed a novel and simple approach with multicolor stimulated Raman scattering microscopy to evaluate rapid DNA imaging, which can be applied to both in vivo DNA dynamic studies and instant label-free human skin cancer diagnosis.

Author contributions: F.L., S.B., C.W.F., D.E.F., and X.S.X. designed research; F.L., S.B., and V.I. performed research; M.J., D.F., and G.R.H. contributed new reagents/analytic tools; F.L., S.B., M.P.H., V.A.N., D.E.F., and X.S.X. analyzed data; and F.L., S.B., D.E.F., and X.S.X. wrote the paper.

Reviewers: D.C., Université Laval; and H.R., Institut Fresnel.

Conflict of interest statement: C.W.F and X.S.X are cofounders of Invenio Imaging, Inc., USA. All other authors declare no conflict of interest.

[1]F.L. and S.B. contributed equally to this work.

[2]Present address: Department of Biochemistry, University of Cambridge, Cambridge CB2 1GA, United Kingdom.

[3]Present address: Invenio Imaging, Inc., Menlo Park, CA 94025.

[4]To whom correspondence may be addressed. Email: dfisher3@mgh.harvard.edu or xie@chemistry.harvard.edu.

This article contains supporting information online at www.pnas.org/lookup/suppl/doi:10.1073/pnas.1515121112/-/DCSupplemental.

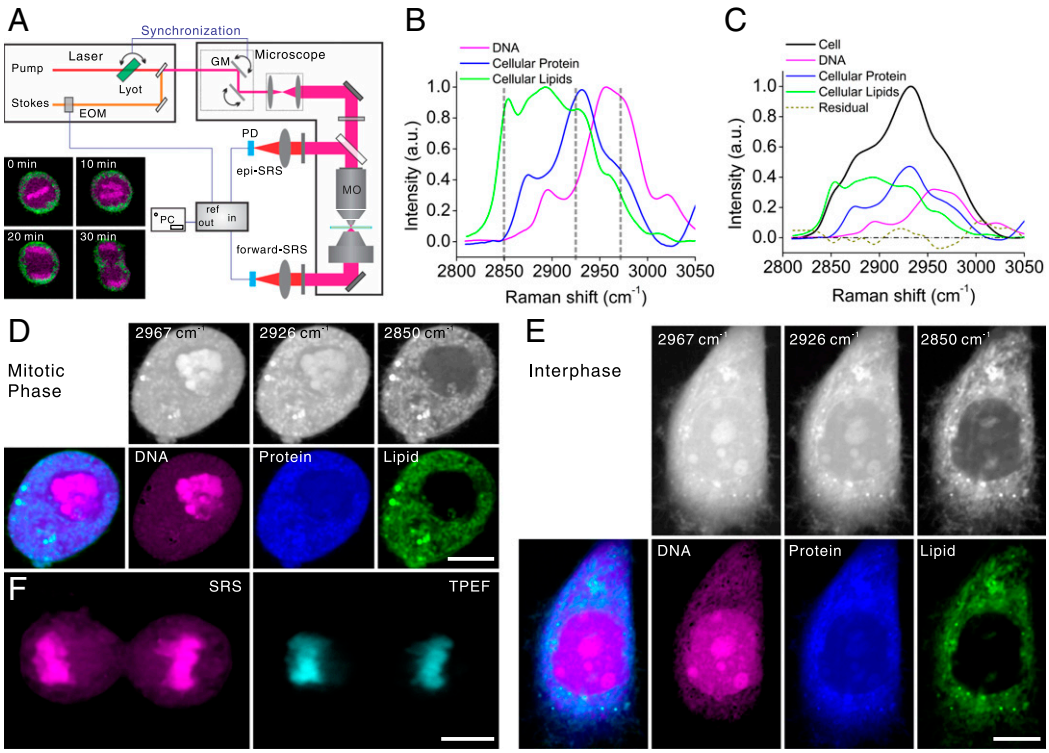

Fig. 1. Label-free SRS imaging of DNA (magenta), protein (blue), and lipids (green) in live cells. SRS images at three selected Raman shifts in the CH stretching vibrational band were acquired. Linear decomposition was performed with a premeasured calibration matrix to retrieve the distribution of DNA, protein, and lipids. (*A*) Setup of the SRS microscopy, capable of automatically acquiring images at multiple Raman shifts. This was achieved by synchronizing the tuning of the laser frequency (Lyot filter) to the imaging frame trigger of the microscope. (*Inset*) Time-lapse images of a HeLa cell undergoing cell division (Movie S1). (*B*) Raman spectra of DNA, cellular protein, and cellular lipids extracted from HeLa cells. (*C*) Raman spectrum of the cell pellet. Linear fitting demonstrated that the three compounds in *B* accounted for ~90% of the total CH stretching vibration of the cells. (*D*) SRS images of a live cell in mitotic phase (prophase) at 2,967, 2,926, and 2,850 cm^{-1}, respectively, and the decomposed distribution of DNA, protein, lipids, and the overlay. Chromosomes were visualized with both high contrast and high signal-to-noise ratio. (*E*) SRS images of a live cell in interphase and the decomposed distribution of DNA, protein, lipids, and the overlay. Detailed internal nuclear features were revealed clearly. (*F*) Images with SRS and TPEF of a mitotic cell stained with DRAQ5, correlated very well with each other. (Scale bar, 10 μm.)

Here we demonstrate that, relying on the unique and distinct spectral features of DNA in the CH stretching vibrational region (the high wavenumber range), the distribution of DNA, together with those of protein and lipids, can be mapped by the linear decomposition of images at three optimally selected Raman shifts. This approach offers much higher sensitivity than that of DNA imaging in the fingerprint region, making dynamic imaging of DNA feasible for both mitotic phase and interphase cells in vitro and in vivo.

Results and Discussion

Multicolor SRS with Linear Decomposition. Noting that SRS and spontaneous Raman spectra are mostly identical (24), the feasibility of imaging DNA in the CH band is evident from the distinct Raman spectra of DNA, protein, and lipid. In the CH stretching region, the DNA peak frequency (2,956 cm^{-1}) is higher than those of protein (2,931 cm^{-1}) and lipid (2,854 cm^{-1}) (Figs. S1*A* and S2*F*). These assignments were confirmed with the Raman spectra of cellular extractions (Fig. 1*B*). Comparing the Raman spectra of deoxyribose phosphate, adenine, thymine, guanine, and cytosine (Fig. S2 *A–E*), we realized that the DNA's CH vibrational signal comes primarily from the deoxyribose. We attributed the blue shift of DNA's CH peak from the protein and lipid peaks to the fact that there are more carbon atoms in deoxyribose than are in proteins and lipids bonded to oxygen atoms, which are more electronegative.

We tested SRS imaging with an artificial sample composed of DNA fibers, BSA as the protein source, immersed in a drop of oleic acid (OA) as the lipid component. For these three components, we acquired three SRS images at three Raman shifts to map the distribution of each compound by linear decomposition. The optimal Raman shifts were selected by theoretical calculation based on the Raman spectra (*Materials and Methods*). SRS images were automatically acquired in tandem through synchronizing the tuning of the laser wavelength to the frame trigger of the microscope. Next, linear decomposition was performed using a premeasured calibration matrix. The distribution of the DNA fiber, protein crystal, and oleic acid were mapped and the three compounds were spatially separated with the expected contents on prior knowledge of the sample (Fig. S1 *B–E*). Thus, this experiment has provided a proof-of-principle to our method (linear decomposition of multicolor SRS imaging). This approach avoids full spectra data acquisition and statistical analysis, offering rapid SRS imaging with multiple chemical contrasts and relatively lower photodamage.

In addition to these major components of interest, the existence of other unknown or ignored components may reduce the accuracy of the linear decomposition. However, when their signal contribution to the total signal is little, then they can be considered to be negligible. Linear fitting of the Raman spectra of DNA, cellular proteins, and lipids (Fig. 1*B*) to the spectrum of a cell pellet, suggested that these three major compounds account for ~90% of the total of the CH stretching vibration of the cells (Fig. 1*C* and *SI Text*), indicating that the overall accuracy of our approach is remarkable and could be used to study biological samples.

Label-Free DNA Imaging in Live Cells. We proceeded with simultaneous imaging of DNA, protein, and lipid in live cells (*Materials and Methods* and Fig. S3*A*). We started from imaging cells in mitotic phase (prophase) with condensed chromosomes undergoing cell division. SRS images at three Raman shifts (2,967, 2,926,

and 2,850 cm^{-1}) were acquired following the approach described above. After linear decomposition, the distribution of nucleic acids, proteins, and lipids were mapped (Fig. 1*D*). Chromosomal DNAs were visualized based on nucleic acids contrast with a high sensitivity. By the optical sectioning capability of SRS, we reconstructed a 3D codistribution of DNA and lipids in a single cell (Fig. S4*A*), showing that, although lipids are widely distributed throughout the cell cytoplasm, their density within the cell nucleus is very low, as expected. Protein distribution appears to be more uniform throughout the entire cell.

We next imaged interphase cells and were able to obtain DNA contrast with a high signal-to-noise ratio (Fig. 1*E*). Chromatin structures within the cell nuclei such as nucleoli, heterochromatin, and euchromatin were visualized at the optical diffraction-limited resolution, demonstrating that SRS imaging of DNA in the CH band offers higher sensitivity than that of the fingerprint spectral region (22).

We were also able to capture chromosome dynamics during in vitro cell division by time-lapse SRS imaging. The chromosomes in a metaphase cell are organized along a line in the center of the cell and then are equally split into two parts as the cell enters in anaphase (Fig. 1*A*, Fig. S3*A*, and Movie S1). SRS imaging captured these different chromosomal dynamics without inducing obvious photodamage to the live cells, as evidenced by the fact that metaphase cells could finish their natural division process with successful passage through the critical M-checkpoint. This experiment demonstrates that label-free live cell imaging with SRS is a powerful method to examine chromosome dynamics during cell division. With this approach, it is also possible to observe nucleolus disassembly and reassembly, to determine the condensation level of DNA, and to monitor the movement of the chromosome during cell division, as well as other crucial cellular processes (25).

Noteworthy, we observed that there is minimal cross-talk among the three decomposed images of DNA, protein, and lipid, demonstrating a good decomposition of molecular compounds. The cell nuclei are clearly visualized with a positive contrast from the DNAs, whereas the ribosomal RNAs are mainly distributed in the cytoplasm, contributing only as a weak background (Fig. 1 *D* and *E* and *SI Text*). To verify the SRS chemical contrast for DNA, we first imaged the cells with SRS and then labeled the cells with a DNA fluorescent dye (DRAQ5) for two-photon excited fluorescence (TPEF) imaging, showing that the paired images matched well with each other (Fig. 1*F*).

Label-Free DNA Imaging for in Vivo Mitotic Counting. We conducted in vivo SRS imaging of DNA in mouse skin to follow cell division activity. 12-0-Tetradecanoylphorbol-13-acetate (TPA) is a potent tumor promoter that has been used to induce epidermal carcinogenesis. Topical treatment of mouse skin with TPA induces epidermal hyperplasia, characterized by significant increase in skin thickness and mass, total number of the cell nuclei, and mitotic rate (26), thus offering an ideal model to study chromosomal dynamics during cell division. Although the proliferative effect of TPA on the mouse skin has been reported, detailed cell cycle kinetics of this process has not yet been well studied due to the lack of proper tools to visualize DNA in vivo.

We therefore performed an in vivo imaging of TPA-treated mouse skin using a skinfold chamber model (*Materials and Methods* and Fig. S3 *B* and *C*). We found that the number of mitotic cells was significantly increased in the epidermis (yellow arrowheads in Fig. 2*A*) with respect to their control counterparts (Fig. 2*B*). This mitotic cell state was easily identified based on stronger DNA signals (Fig. 2*D*), as well as its distinctive morphology of condensed chromosomes, compared with a cell nucleus in interphase (Fig. S4*B*). Fig. 2*C* shows representative images of cell nuclei at different stages of a complete cell cycle, in which nuclear morphology, including internal detailed structures, was clearly visualized. In addition, unlike in vitro cultured cells, very few lipid droplets were observed in live mouse skin tissue. Fluorescent staining was used to confirm the DNA contrast of SRS in intact fresh skin tissue (Fig. S4*C*). We also captured the dynamic of a cancer cell during division by recording an in vivo SRS movie with the same skinfold chamber on an immune-deficient mice injected with human cancer cells to create a xenograft model (*Materials and Methods*). The splitting of the chromosomes was easily seen when the cell was entering anaphase, by using time-lapse SRS imaging based on DNA contrast (Movie S2).

We then tracked the cell cycle kinetics during the proliferation process through performing in vivo mitotic counting in TPA-treated mouse skin, by applying time-lapse SRS imaging based on DNA contrast (*Materials and Methods* and Figs. S3*D* and S5). Fig. 2*E* shows the mitotic rates (number of mitotic cells per thousand cells) over a 24-h period with a 6-h interval. Our data show that mitotic activity reached a peak at ∼18 h and then decreased at ∼24 h (Figs. S6–S9). This result confirmed that a synchronized wave of basal cell proliferation is induced by TPA in adult mouse skin. We noted that in vivo SRS imaging of DNA makes this type of dynamic studies possible because of its unique proficiencies, including label-free intrinsic chemical contrast, high sensitivity, and 3D sectioning capability, with no photo bleaching.

In addition, SRS offers the possibility of label-free imaging of live cancer cells from primary tumors, which is difficult to label with fluorescence without perturbing cell functions. We anticipate important clinical applications of this approach, such as assessing and screening morphologic effects of antineoplastic agents in real time (27). For in vivo imaging of live animals, a modified skinfold chamber model was used, and a subskin implantation model was developed to minimize the breathing motion artifacts in our experiments, which could also be applied for other microscopic imaging modalities. Future SRS technical developments, such as simultaneous multicolor imaging, video rate scanning, and the design of endoscopic or handheld probes, will further release the critical requirements to the animal immobilization strategies.

Label-Free SRS Histology for Human Skin Cancer Diagnosis. We broadened the use of SRS to image human skin tissue. The nuclear morphology in normal human skin was clearly visualized with positive DNA contrast with a high sensitivity, as well as images of protein and lipids, which displayed the regularly layered skin structures (Fig. 3 *A* and *B*), providing complementary tissue and cellular morphological information. To first validate the DNA contrast in human tissue, we imaged the same skin tissue section with SRS and H&E staining in tandem. We found a clear correlation in terms of visibility of detailed nuclear morphology and architecture, as well as cellular and tissue morphology (Fig. 3 *C* and *D*), confirming the effectiveness of our method.

To demonstrate the potential of SRS for label-free histology of cancer in humans, we imaged fresh human skin cancer tissue from three surgical cases of squamous cell carcinoma (SCC), the second most common type of skin cancer (28). We found that we could easily identify an increased number of mitotic figures based on stronger signals and distinctive morphological features of the condensed chromosomes (yellow arrowheads in Fig. 3*E*) (29). Mitotic figures are valuable diagnostic and prognostic indicators of cancer aggressiveness (30), becausew it correlates directly with the level of cell division and proliferation. Fig. 3*F* shows another representative image of a small nest of carcinoma cells, in which aggregated tumor cells with enlarged nuclei (right side of the dotted curve) are surrounded by nonneoplastic cells with smaller nuclei (left side of the curve), reflecting high intratumoral heterogeneity (31). Our results demonstrate that the multicolor SRS approach for label-free imaging of DNA, protein, and lipids in tissues offers clear and equivalent histological features as conventional H&E staining does for skin cancer diagnosis, with the advantage of being a label-free method and thus not affecting the native form of the tissue.

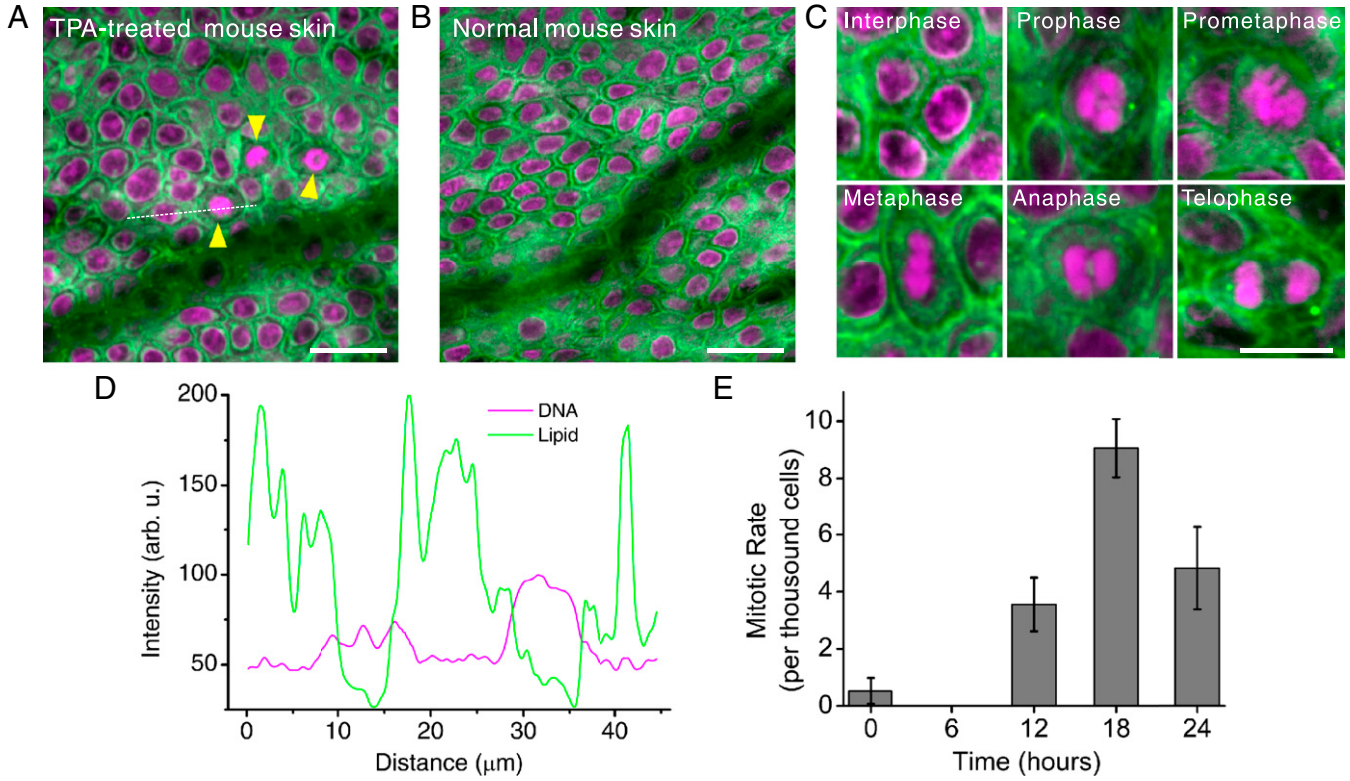

Fig. 2. Label-free in vivo SRS imaging of DNA (magenta) and lipids (green) in the mouse skin and in vivo mitotic counting. (*A*) SRS images of the TPA-treated mouse skin showed increased numbers of the mitotic figures (yellow arrowheads). The nuclear morphology of cells in interphase and mitotic phase were easily distinguishable. (*B*) SRS images of untreated mouse skin barely showed mitosis. (*C*) Representative SRS images of epidermal keratinocytes in the TPA-treated mouse skin at different stages of the whole cell cycle: interphase, prophase, prometaphase, metaphase, anaphase, and telophase. (*D*) Intensity profile across the dotted line in *A*. The DNA contrast in a mitotic cell (~2:1) is higher than that of the cell nuclei in interphase (~1.4:1). (*E*) Tracking the cell division activity through in vivo counting of the mitotic rates of the basal keratinocytes in the TPA-treated mouse skin over 24 h. The total number of cells counted was ~5,000 (Figs. S6–S9). (Scale bar, 20 μm.)

Although other multiphoton imaging techniques such as native TPEF and second harmonic generation (SHG) can also reveal most of the tissue morphological features (32, 33), SRS provides chemical specificity for nucleic acids. SRS therefore highlights both the nuclear morphology and also allows for quantification, enabling identification of mitoses and nuclear atypia in a quantitative fashion. We expect that SRS histology may not only speed up Mohs surgery by on-site label-free imaging of tumor tissue with margins, but also has the potential for in vivo noninvasive detection and progress evaluation of skin lesions in real time.

Materials and Methods

SRS Microscopy. We used the picoEMERALD laser source (APE), which comprises an optical parametric oscillator (OPO) synchronously pumped by a frequency-doubled picosecond oscillator (High-Q Laser) in a single housing. The OPO supplies the pump beam (5–6 ps, tunable from 720 to 990 nm), and the oscillator supplies the Stokes beam (7 ps, 1,064 nm). The two beams are temporally synchronized and spatially overlapped and then are coupled into a modified laser-scanning confocal microscope (FV300; Olympus) for SRS imaging. This picosecond system maps the sample of a single Raman shift at a time. To do spectral or multicolor imaging, the wavelength of the pump beam is scanned by tuning the Lyot filter in the OPO cavity. In our experiment, we synchronized the tuning of the Lyot filter to the frame trigger of the microscope through the RS232 serial port by Labview programming to realize automatic image acquisition at optimally selected multiple Raman shifts frame by frame, which made our multicolor SRS microscope feasible for long-term time-lapse imaging of live cells and live animals in vivo. Each frame (512×512) was taken recurrently within 1 s to a few seconds. We used a high NA water immersion objective lens for imaging (UPlanApo IR 60× NA 1.2; Olympus).

Optimal Wavelength Selection. We used an artificial sample to demonstrate the multicolor approach with linear decomposition. The sample was composed of DNA fibers (Sigma) and a piece of BSA crystal (representing protein; Sigma), immersed in a droplet of oleic acid (OA, representing lipid; Sigma). Mathematically, for three components, at least three images should be acquired at three Raman shifts. The Raman spectra of DNA, BSA, and OA in the high wavenumber range of the carbon-hydrogen (CH) stretching vibrational band (2,800–3,050 cm^{-1}) are shown in Fig. S1*A*. Although they largely overlap, they clearly do show distinct spectral features. As the spectra of SRS and Raman are mostly identical, to select the most distinct spectral features to decompose the three components (DNA, BSA, and OA) with as much accuracy as possible, we performed a simulation based on the criterion that minimizing the root mean square error (RMSE) between the concentrations of the mixture components and their estimates to select the optimal Raman shifts (34–36).

For a sample containing M components with unknown concentrations $\{c_m | m = 1...M\}$, respectively, we measure SRS signals at N wavelengths $\{\omega_n | n = 1...N\}$ ($N \geq M$). The optimal wavelengths can be determined by minimizing the RMSE between the true concentration and the calculated concentration

$$\mathrm{RMSE} = \sqrt{tr\left\{E\left[(c-\hat{c})(c-\hat{c})^t\right]\right\}} \rightarrow \min, \quad [1]$$

where tr, E, and t denote matrix trace, expectation, and transpose, respectively. The measured spectrum $\{S_n\}$ is equal to the linear combination of the spectra of the M components $\{k_m(\omega_n)\}$ weighted by the concentrations and the detection noise $\{r(\omega_n)\}$

$$S = Kc + r, \quad [2]$$

where

$$S = \begin{bmatrix} S(\omega_1) \\ \vdots \\ S(\omega_N) \end{bmatrix}, c = \begin{bmatrix} c_1 \\ \vdots \\ c_M \end{bmatrix}, r = \begin{bmatrix} r(\omega_1) \\ \vdots \\ r(\omega_N) \end{bmatrix},$$

and

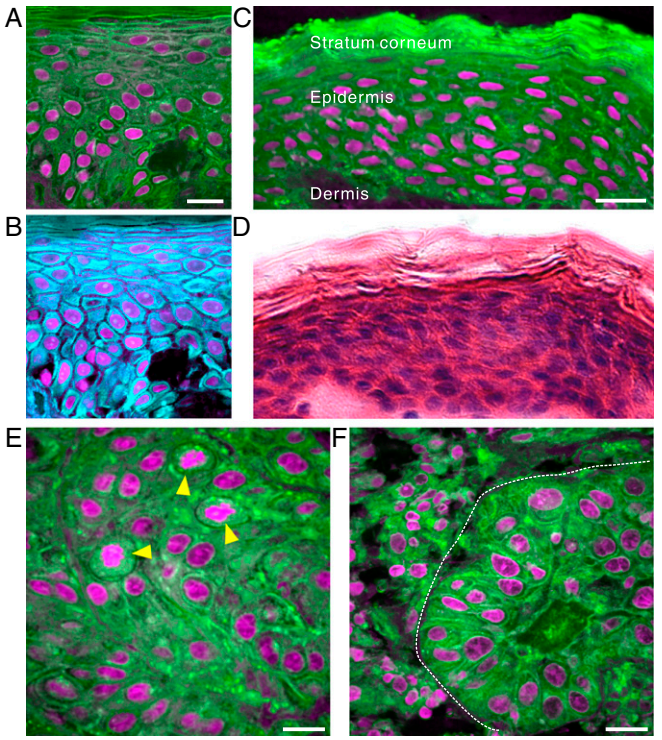

Fig. 3. SRS images of DNA (magenta), protein (cyan), and lipids (green) in human skin and skin cancer tissue. (*A*) Codistribution of DNA with lipids and (*B*) DNA with protein of fresh-frozen sectioned normal human skin tissue. Both nuclear and tissue morphology were clearly visualized. (*C* and *D*) Paired images of SRS and H&E of the same normal human skin tissue section verified that SRS provides equivalent cytologic features to H&E staining. (*E*) SRS images of fresh human skin squamous cell carcinoma (SCC) tissue showed increased number of the mitotic figures. (*F*) SRS images of a small nest of carcinoma cells with enlarged cell nuclei in comparison with adjacent non-neoplastic cells. Thickness of the frozen sections for *A*–*D* is ∼20 μm. Thickness of the fresh tissue for *E* and *F* is ∼1 mm. (Scale bar, 20 μm.)

$$K = \begin{bmatrix} k_1(\omega_1) & \cdots & k_M(\omega_1) \\ \vdots & & \vdots \\ k_1(\omega_N) & \cdots & k_M(\omega_N) \end{bmatrix}.$$

The least square solution for Eq. **2** is

$$\hat{c} = K^{-1}S. \qquad [3]$$

Substituting Eqs. **2** and **3** to Eq. **1** yields

$$\mathrm{RMSE} = \sqrt{tr\left[K^{-1}E(rr^t)(K^t)^{-1}\right]}. \qquad [4]$$

Given that the detection noise in SRS imaging is near shot-noise limited and obeys an uncorrelated process with zero mean and a constant variance σ^2, Eq. **4** reduces to

$$\mathrm{RMSE} = \sigma \cdot \sqrt{tr\left[(K^tK)^{-1}\right]}, \qquad [5]$$

where the calibration matrix *K* was based on the Raman spectra of the pure chemicals. Our simulations using Eqs. **1** and **5** allowed the selection of three optimal Raman shifts at 2,973, 2,921, and 2,851 cm^{-1} (Fig. S1).

Spontaneous Raman Spectroscopy. The Raman spectra were acquired using a confocal Raman spectrometer (LabRAM HR800; Horiba Jobin Yvon). A Helium-Neon (HeNe) laser at 633 nm was used to excite the sample. The spectra were processed using LabSpec software. The objective is RMS20X (Olympus: NA, 0.4, WD, 1.2 mm). The average power on the sample was ∼20 mW. Integration time for each spectra was ∼10–30 s.

TPEF Microscopy. TPEF imaging of DNA stained with DRAQ5 (BioStatus) in live cells and tissue was excited by the 1,064-nm beam (by blocking the OPO beam) and detected by a photomultiplier tube (PMT; Hamamatsu) through a dichroic mirror and a short-pass filter. The samples were first imaged with SRS and then were stained with DRAQ5 (10 μM, 10 min for live cells and 30 min for fresh tissue at room temperature) directly on the microscopy stage (37).

Cell Culture. HeLa S3 cells (ATCC) were maintained at 37 °C in a humidified 5% (vol/vol) CO_2 air incubator and cultured in MEM (Invitrogen) supplemented with 10% (vol/vol) FBS and 0.01 mg/mL insulin (Sigma). Cells were imaged in phenol red-free MEM (Sigma) supplemented with sodium bicarbonate, 20 mM L-glutamine,100 ng/mL epidermal growth factor (EGF; Sigma), and 25 mM Hepes, pH 8.0 (Invitrogen).

Time-lapse imaging of live cells for observing the cell division process was carried out on a 35-mm dish with a 0.17-mm coverglass bottom (MatTek) in a modified onstage incubator (Live Cell Instrument; Chamlide). To accommodate both high NA objective and high NA condenser with very short working distance (<1 mm) for SRS imaging, the upper cover of the incubator was specifically designed using flexible plastic materials to enclose the objective within the incubator and to allow it to move for aligning and focusing at the same time (Fig. S3*A*). The temperature was maintained at 37 °C with 5% (vol/vol) CO_2 in humidified air. An extra 35-mm dish with 1× PBS solution was placed within the incubator for better humidity maintenance.

For in vitro cell division imaging, HeLa cells were synchronized by double thymidine block (38). This procedure involved 18-h incubation (prepared at ∼25–30% confluence) in thymidine (final concentration, 2 mM; Sigma), 9-h incubation in fresh media, and again a 17-h incubation in thymidine (final concentration, 2 mM). Before imaging, cells were incubated in fresh media for 8 h to allow cells reach middle G2 phase. For in vivo cell division imaging in the xenograft mouse model, HeLa cells were also synchronized using double thymidine block. After releasing, incubated cells in fresh media for 3 h before injecting into the mouse skinfold chamber. The total cellular lipids from the cultured HeLa cell pellet were extracted using the Bligh-Dyer method (39). Total cellular protein was extracted using RIPA buffer (Thermo Scientific). We did not extracted DNA from the cell pellet.

Dorsal Skinfold Chamber Model in Mice. To minimize the motion artifacts in live animal imaging with multicolor SRS, we built the dorsal skinfold chamber model on mice. The skinfold chamber, which consists of two symmetrical titanium frames, was implanted in the dorsal skin of the mice following previously reported procedures (40–42). The chamber sandwiched and immobilized the skin on the back of the mouse. One side of the skin was surgically removed and replaced by a round 0.17-mm coverglass with a 10-mm diameter. The screws used should be as short as possible on both sides of the chamber to allow the high NA objective and the high NA condenser to be able to access to the chamber as close as needed for SRS transmission imaging (Fig. S3 *B* and *C*). We used this model for two experiments as follows. (*i*) For the experiment of in vivo mouse skin imaging, young adult mice (Swiss Webster, female, 6 wk; Taconic) were used. The skin within the chamber was topically treated with 2 μg TPA (Sigma) in 200 μL acetone to activate cell division activity (26, 43, 44). (*ii*) For in vivo cell division dynamic imaging experiments, Ncr nude female mice (Taconic) were used to establish a xenograft model (45, 46). Synchronized HeLa cells with double thymidine block were injected into the chamber superficially beneath the inner side of the skin. Images were taken after 26 h of the injection.

Mouse Subskin Implantation Model for in Vivo Epi-SRS Imaging. Mouse dorsal skin was topically treated with 8 μg TPA in 800 μL acetone to activate cell division activity in the skin. To immobilize the skin for imaging, a thin metal piece was surgically implanted under the skin (titanium, 12 × 12 × 1 mm) with two small handles (2 × 5 × 1 mm) extended out of the skin. When imaging, the two small handles were fixed to a mounting block on the microscope stage with the mouse under anesthesia. After imaging, the mouse was released and maintained in the cage in normal conditions. All of the in vivo animal experiments were performed under standard anesthesia condition using O_2/isoflurane (Fig. S3*D*). Animal experiments were conducted in accordance with Harvard University IACUC Protocols 10-02 and 29-01.

Human Skin and Skin Cancer Tissue. Discarded and deidentified human skin samples including normal (from five surgical cases) and SCC (from three surgical cases) tissue were collected and prepared in accordance with Massachusetts General Hospital institutional review board protocol 2013-P-2337.

To collect paired images with SRS and H&E from the same tissue slice, fresh normal skin tissue was quickly embedded and frozen in OCT compound for frozen sectioning without fixation; 20-μm slices were first imaged with SRS and then were stained with H&E (following standard procedures) for light microcopy imaging. Fresh SCC tissue was cut into thin slices using a blade (~1 mm) and then was sandwiched between a slide and coverglass for SRS transmission imaging. Some pressure was applied to flatten the tissue.

ACKNOWLEDGMENTS. We thank Dr. X. Ni, Dr. X. Zhang, and Dr. J. Yong for help on the animal experiments; W. Yang for technical assistance on the photo detector; Dr. L. Sang, Dr. L. Kong, Dr. A. J. Golby, and Dr. N. Y. Agar for helpful discussions; and Dr. D. Lando and Dr. P. Purcell for critical reading and editing of the manuscript. This work was supported by grants to X.S.X. from the US Department of Energy's Basic Energy Sciences Program (DE-FG02-09ER16104) and National Institutes of Health (NIH) T-R01 (1R01EB010244-01) and to D.E.F. from the Dr. Miriam and Sheldon G. Adelson Medical Research Foundation and the NIH (P01 CA163222, R01 AR043369, and R21 CA175907).

1. Kagey MH, et al. (2010) Mediator and cohesin connect gene expression and chromatin architecture. *Nature* 467(7314):430–435.
2. Apostolou E, Hochedlinger K (2013) Chromatin dynamics during cellular reprogramming. *Nature* 502(7472):462–471.
3. Jannink I, Risberg B, Van Diest PJ, Baak JPA (1996) Heterogeneity of mitotic activity in breast cancer. *Histopathology* 29(5):421–428.
4. Aasi SZ, Leffel DJ, Lazova RZ (2012) *Atlas of practical mohs histopathology* (Springer, New York).
5. Freudiger CW, et al. (2008) Label-free biomedical imaging with high sensitivity by stimulated Raman scattering microscopy. *Science* 322(5909):1857–1861.
6. Nandakumar P, Kovalev A, Volkmer A (2009) Vibrational imaging based on stimulated Raman scattering microscopy. *New J Phys* 11:033026.
7. Ideguchi T, et al. (2013) Coherent Raman spectro-imaging with laser frequency combs. *Nature* 502(7471):355–358.
8. Berto P, Andresen ER, Rigneault H (2014) Background-free stimulated Raman spectroscopy and microscopy. *Phys Rev Lett* 112(5):053905.
9. Bégin S, Bélanger E, Laffray S, Vallée R, Côté D (2009) In vivo optical monitoring of tissue pathologies and diseases with vibrational contrast. *J Biophotonics* 2(11): 632–642.
10. Saar BG, et al. (2010) Video-rate molecular imaging in vivo with stimulated Raman scattering. *Science* 330(6009):1368–1370.
11. Ji M, et al. (2013) Rapid, label-free detection of brain tumors with stimulated Raman scattering microscopy. *Sci Transl Med* 5(201):201ra119.
12. Mittal R, et al. (2013) Evaluation of stimulated Raman scattering microscopy for identifying squamous cell carcinoma in human skin. *Lasers Surg Med* 45(8):496–502.
13. Fu D, et al. (2014) Imaging the intracellular distribution of tyrosine kinase inhibitors in living cells with quantitative hyperspectral stimulated Raman scattering. *Nat Chem* 6(7):614–622.
14. Wei L, et al. (2014) Live-cell imaging of alkyne-tagged small biomolecules by stimulated Raman scattering. *Nat Methods* 11(4):410–412.
15. Yue S, et al. (2014) Cholesteryl ester accumulation induced by PTEN loss and PI3K/AKT activation underlies human prostate cancer aggressiveness. *Cell Metab* 19(3):393–406.
16. Freudiger CW, et al. (2011) Highly specific label-free molecular imaging with spectrally tailored excitation stimulated Raman scattering (STE-SRS) microscopy. *Nat Photonics* 5(2):103–109.
17. Fu D, et al. (2012) Quantitative chemical imaging with multiplex stimulated Raman scattering microscopy. *J Am Chem Soc* 134(8):3623–3626.
18. Ozeki Y, et al. (2012) High-speed molecular spectral imaging of tissue with stimulated Raman scattering. *Nat Photonics* 6(12):844–850.
19. Wang K, et al. (2013) Time-lens based hyperspectral stimulated Raman scattering imaging and quantitative spectral analysis. *J Biophotonics* 6(10):815–820.
20. Freudiger CW, et al. (2012) Multicolored stain-free histopathology with coherent Raman imaging. *Lab Invest* 92(10):1492–1502.
21. Lu FK, et al. (2012) Multicolor stimulated Raman scattering (SRS) microscopy. *Mol Phys* 110(15-16):1927–1932.
22. Zhang X, et al. (2012) Label-free live-cell imaging of nucleic acids using stimulated Raman scattering microscopy. *ChemPhysChem* 13(4):1054–1059.
23. Klein K, et al. (2012) Label-free live-cell imaging with confocal Raman microscopy. *Biophys J* 102(2):360–368.
24. Cheng J-X, Xie XS (2013) *Coherent Raman scattering microscopy* (CRC Press, Boca Raton).
25. Jeppsson K, Kanno T, Shirahige K, Sjögren C (2014) The maintenance of chromosome structure: Positioning and functioning of SMC complexes. *Nat Rev Mol Cell Biol* 15(9): 601–614.
26. Rodriguez-Puebla ML, Robles AI, Johnson DG, LaCava M, & Conti CJ (1998) Synchronized proliferation induced by 12-O-tetradecanoylphorbol-13-acetate treatment of mouse skin: An in vivo model for cell cycle regulation. *Cell growth & differentiation: the molecular biology journal of the American Association for Cancer Research* 9(1):31-39.
27. Tentler JJ, et al. (2012) Patient-derived tumour xenografts as models for oncology drug development. *Nat Rev Clin Oncol* 9(6):338–350.
28. Madan V, Lear JT, Szeimies RM (2010) Non-melanoma skin cancer. *Lancet* 375(9715): 673–685.
29. Petter G, Haustein UF (1998) Squamous cell carcinoma of the skin–histopathological features and their significance for the clinical outcome. *J Eur Acad Dermatol Venereol* 11(1):37–44.
30. Warner CL, Cockerell CJ (2011) The new seventh edition American Joint Committee on Cancer staging of cutaneous non-melanoma skin cancer: A critical review. *Am J Clin Dermatol* 12(3):147–154.
31. Marusyk A, Almendro V, Polyak K (2012) Intra-tumour heterogeneity: A looking glass for cancer? *Nat Rev Cancer* 12(5):323–334.
32. Konig K, Riemann I (2003) High-resolution multiphoton tomography of human skin with subcellular spatial resolution and picosecond time resolution. *J Biomed Opt* 8(3): 432–439.
33. Chen X, Grégoire S, Formanek F, Galey JB, Rigneault H (2015) Quantitative 3D molecular cutaneous absorption in human skin using label free nonlinear microscopy. *J Control Release* 200:78–86.
34. Frans SD, Harris JM (1985) Selection of Analytical Wavelengths for Multicomponent Spectrophotometric Determinations. *Anal Chem* 57(13):2680–2684.
35. Sasaki K, Kawata S, Minami S (1986) Optimal Wavelength Selection for Quantitative-Analysis. *Appl Spectrosc* 40(2):185–190.
36. Osborne SD, Jordan RB, Kunnemeyer R (1997) Method of wavelength selection for partial least squares. *Analyst (Lond)* 122(12):1531–1537.
37. Martin RM, Leonhardt H, & Cardoso MC (2005) DNA labeling in living cells. *Cytometry. Part A: the journal of the International Society for Analytical Cytology* 67(1):45-52.
38. Peng CY, et al. (1997) Mitotic and G2 checkpoint control: Regulation of 14-3-3 protein binding by phosphorylation of Cdc25C on serine-216. *Science* 277(5331):1501–1505.
39. Bligh EG, Dyer WJ (1959) A rapid method of total lipid extraction and purification. *Can J Biochem Physiol* 37(8):911–917.
40. Papenfuss HD, Gross JF, Intaglietta M, Treese FA (1979) A transparent access chamber for the rat dorsal skin fold. *Microvasc Res* 18(3):311–318.
41. Huang Q, et al. (1999) Noninvasive visualization of tumors in rodent dorsal skin window chambers. *Nat Biotechnol* 17(10):1033–1035.
42. Palmer GM, et al. (2011) In vivo optical molecular imaging and analysis in mice using dorsal window chamber models applied to hypoxia, vasculature and fluorescent reporters. *Nat Protoc* 6(9):1355–1366.
43. Slaga TJ, Fischer SM, Weeks CE, Klein-Szanto AJ, Reiners J (1982) Studies on the mechanisms involved in multistage carcinogenesis in mouse skin. *J Cell Biochem* 18(1): 99–119.
44. Argyris TS (1980) Epidermal growth following a single application of 12-O-tetradecanoyl-phorbol-13-acetate in mice. *Am J Pathol* 98(3):639–648.
45. Morton CL, Houghton PJ (2007) Establishment of human tumor xenografts in immunodeficient mice. *Nat Protoc* 2(2):247–250.
46. Orth JD, et al. (2011) Analysis of mitosis and antimitotic drug responses in tumors by in vivo microscopy and single-cell pharmacodynamics. *Cancer Res* 71(13):4608–4616.
47. Puppels GJ, et al. (1990) Studying single living cells and chromosomes by confocal Raman microspectroscopy. *Nature* 347(6290):301–303.
48. Thomas GJ, Jr (1999) Raman spectroscopy of protein and nucleic acid assemblies. *Annu Rev Biophys Biomol Struct* 28:1–27.
49. Huang Z, et al. (2003) Near-infrared Raman spectroscopy for optical diagnosis of lung cancer. *Int J Cancer* 107(6):1047–1052.
50. Uzunbajakava N, et al. (2003) Nonresonant confocal Raman imaging of DNA and protein distribution in apoptotic cells. *Biophys J* 84(6):3968–3981.
51. Jess PR, *et al*. (2007) Early detection of cervical neoplasia by Raman spectroscopy. *International journal of cancer. Journal international du cancer* 121(12):2723-2728.
52. Chowdary MV, et al. (2009) Biochemical correlation of Raman spectra of normal, benign and malignant breast tissues: A spectral deconvolution study. *Biopolymers* 91(7):539–546.
53. Jachtenberg JW, et al. (2013) Raman spectroscopy can discriminate distinct glioma subtypes as defined by RNA expression profiling. *J Raman Spectrosc* 44(9):1217–1221.
54. Chen Y, et al. (2014) Raman spectroscopy analysis of the biochemical characteristics of molecules associated with the malignant transformation of gastric mucosa. *PLoS One* 9(4):e93906.
55. Okotrub KA, Surovtsev NV, Semeshin VF, & Omelyanchuk LV (2015) Raman spectroscopy for DNA quantification in cell nucleus. *Cytometry. Part A: the journal of the International Society for Analytical Cytology* 87(1):68-73.
56. Parker FS (1983) *Applications of Infrared, Raman, and Resonance Raman Spectroscopy in Biochemistry* (Plenum Press, New York).
57. Matthäus C, Boydston-White S, Miljković M, Romeo M, Diem M (2006) Raman and infrared microspectral imaging of mitotic cells. *Appl Spectrosc* 60(1):1–8.
58. Mallidis C, et al. (2011) In situ visualization of damaged DNA in human sperm by Raman microspectroscopy. *Hum Reprod* 26(7):1641–1649.
59. Fu D, Xie XS (2014) Reliable cell segmentation based on spectral phasor analysis of hyperspectral stimulated Raman scattering imaging data. *Anal Chem* 86(9):4115–4119.
60. Liao C-S, et al. (2015) Microsecond scale vibrational spectroscopic imaging by multiplex stimulated Raman scattering microscopy. *Light Sci Appl* 4:e265.